Dopant-induced Morphology of Organic Semiconductors Resulting in High Doping Performance

Jing Guo, Ping-an Chen, Shuzhang Yang, Huan Wei, Yu Liu, Jiangnan Xia, Chen Chen, Huajie Chen, Suhao Wang, Wenwu Li, et al.

Dopant-induced Morphology of Organic Semiconductors Resulting in High Doping Performance

Jing Guo[1,2], Ping-An Chen[1,3,4], Shuzhang Yang[5], Huan Wei[3,4], Yu Liu[3,4], Jiangnan Xia[3,4], Chen Chen[6], Huajie Chen[7], Suhao Wang[8], Wenwu Li[5], Yuanyuan Hu[1,3,4]*

[1]Changsha Semiconductor Technology and Application Innovation Research Institute, College of Semiconductors (College of Integrated Circuits), Hunan University, Changsha 410082, China

[2]School of Physics and Information Engineering, Shanxi Normal University, Taiyuan 031000, China

[3]Shenzhen Research Institute of Hunan University, Shenzhen 518063, China

[4]International Science and Technology Innovation Cooperation Base for Advanced Display Technologies of Hunan Province, School of Physics and Electronics, Hunan University, Changsha 410082, China

[5]Shanghai Frontiers Science Research Base of Intelligent Optoelectronics and Perception, Institute of Optoelectronics, Department of Materials Science, Fudan University, Shanghai 200433, China.

[6]Science and Technology on Advanced Ceramic Fibers and Composites Laboratory, College of Aerospace Science and Engineering, National University of Defense Technology, Changsha 410000, China

[7]Key Laboratory of Environmentally Friendly Chemistry and Applications of Ministry of Education, College of Chemistry, Xiangtan University, Xiangtan 411105, China

[8] Unité de Dynamique et Structure des Matériaux Moléculaires (UDSMM), Université du Littoral Côte d'Opale, 145 Avenue Maurice Schumann, 59140 Dunkerque, France

Correspondence: yhu@hnu.edu.cn

Abstract:

Doping plays a crucial role in modulating and enhancing the performance of organic semiconductor (OSC) devices. In this study, we underscore the critical role of dopants in shaping the morphology and structure of OSC films, which in turn profoundly influences their properties. Two dopants, trityl tetrakis(pentafluorophenyl) (TrTPFB) and N,N-dimethylanilinium tetrakis(pentafluorophenyl)borate (DMA-TPFB), were examined for their doping effects on P3HT and PBBT-2T host OSCs. It is found that although TrTPFB exhibits higher doping efficiency, OSCs doped with DMA-TPFB achieve comparable or even enhanced electrical conductivity. Indeed, the electrical conductivity of DMA-TPFB doped P3HT reaches over 67 S cm^{-1}, which is a record-high value for mixed-solution-doped P3HT. This can be attributed to DMA-TPFB inducing a higher degree of crystallinity and reduced structural disorder. Moreover, the beneficial impact of DMA-TPFB on the OSC films' morphology and structure results in superior thermoelectric performance in the doped OSCs. These findings highlight the significance of dopant-induced morphological and structural considerations in enhancing the film characteristics of OSCs, opening up a new avenue for optimization of dopant performance.

INTRODUCTION

Doping is crucial not only for inorganic semiconductors, but also for organic semiconductors (OSCs). The electrical properties such as mobility and electrical conductivity can be greatly enhanced by doping, especially for OSCs which are deficient in these intrinsic properties[1-5]. The excellent electrical properties ensure that OSCs can function efficiently in device applications. For example, doping OSCs to enhance their electrical conductivity is a very effective way to improve the performance of organic thermoelectric devices (OTEs)[6-10]. According to the equation of power factor $PF = S^2\sigma$, where S represents the Seebeck coefficient and σ denotes the electrical conductivity, a high electrical conductivity is pursued to achieve large PF value of OTEs, which means that the devices have high thermoelectric conversion efficiency[11, 12]. Therefore, increasing amount of research is focusing on doping to improve the electrical properties of OSCs.

In the study of doping for OSCs, the development of new dopants is undoubtedly the most important part. In the past few years, tremendous efforts have been made to develop more efficient and stable dopants. Taking p-dopants as an example, a variety of dopants have been developed in the past few decades, such as molecular dopants, Lewis acid dopants, and ionic dopants. Molecular dopants, such as TCNQ, F_4TCNQ, F_6TCNNQ and their derivatives[2, 13-16], dope through redox reaction, i.e., the electron transfer between the Highest Occupied Molecular Orbital (HOMO) of the host semiconductor and the Lowest Unoccupied Molecular Orbital (LUMO) of the dopant. Molecular dopants have been investigated with the aim of deepening the LUMO level of the dopants, thus enhancing their doping strength[16, 17]. Lewis acid dopants, such as $B(C_6F_5)$[18, 19], $Zn(C_6F_5)_2$[20, 21], etc., which can dope a wide range of OSCs through the protonation doping mechanism[22, 23], have been under intensive investigations in the last few years. More recently, ionic dopants composed of cations and anions, such as TrTPFB[24-26], $Mes_2B^+[B(C_6F_5)_4]^-$[22] and T-PCCp[27] have attracted increasing attention from researchers. The doping mechanism of such ionic dopants was proposed to be

based on the electrophilic-attack reaction, followed by the electron transfer between attacked molecules and neutral molecules[26]. These ionic dopants are promising dopants as they have shown high doping efficiency, good stability, and universal doping effect for OSCs.

In general, previous studies have mainly focused on enhancing the electron transfer chances between host OSCs and dopants, which fundamentally determine the doping performance or efficiency[28-31]. While significant efforts have been made in improving doping performance through dopant development and understanding new doping mechanisms, the electrical characteristics of doped OSC films are not solely dictated by electron transfer processes. Dopants not only introduce charge carriers into semiconductor films but also induce changes in their morphologies and microstructures, particularly in blended OSC/dopant systems[32]. Studies have demonstrated that dopants can induce notable structural and morphological alterations in doped films[33-35]. These dopant-induced structural changes play a critical role in determining the electrical performance of doped OSC films[36, 37] and their thermoelectric properties[38-40]. The processing methods of doping also significantly impact semiconductor performance by influencing the film's structure and morphology[41-45].

These findings have sparked a novel approach to enhancing dopant performance by optimizing dopant-induced structural changes in OSC films. Specifically, even without enhancing the doping capability, i.e., the electron transfer magnitude between dopants and OSC molecules, high electrical and thermoelectric performance in doped OSC films can be achieved through improved structure and morphology. Implementing this concept would open up diverse opportunities for dopant engineering aimed at developing high-performance dopants.

In this study, we demonstrate the feasibility of this approach by conducting a comparative study of the doping performance of two organic dopants, trityl tetrakis(pentafluorophenyl) (TrTPFB) and N,N-dimethylanilinium tetrakis(pentafluorophenyl)borate (DMA-TPFB), on OSC films. While the doping

effect of the two dopants have been reported by us previously[3, 26], the relationship between dopant structure and performance has not been thoroughly investigated yet. Our investigation revealed that TrTPFB exhibits higher doping efficiency than DMA-TPFB in both P3HT and PBBT-2T host OSCs. Despite this, the electrical conductivity of DMA-TPFB doped OSCs is comparable or even higher than that of TrTPFB doped ones. For instance, the electrical conductivity of DMA-TPFB doped P3HT approaches 70 S cm^{-1}, a record-high value for solution-doped P3HT and significantly higher than that of TrTPFB doped P3HT. Grazing incidence wide angle X-ray scattering (GIWAXS) and atomic force microscopy (AFM) analysis indicates that DMA-TPFB induces higher crystallinity (i.e., lower structural disorder) in the doped films, which is beneficial for charge transport and explains the higher electrical conductivity in these films. Moreover, DMA-TPFB is identified to result in higher thermoelectric performance than TrTPFB in the same host semiconductor, thanks to the beneficial effect of DMA-TPFB on film structures, i.e., the resulted lower disorder in doped films. These results underscore the significance of considering dopant-induced structural changes in OSC films. They reveal that dopants with lower intrinsic doping strength can outperform in terms of semiconductor performance if they induce beneficial morphological changes. This discovery paves the way for a new strategy in enhancing dopant performance by focusing on their impact on film structures.

RESULTS AND DISCUSSION

2.1 Doping effect of TrTPFB and DMA-TPFB

Figure 1a shows two organic salt dopants TrTPFB and DMA-TPFB with similar structures and $TPFB^-$anions in common. These two organic salts have great advantages as organic semiconductor dopants due to their excellent solubility in common organic solvents such as chlorobenzene and chloroform at room temperature. Meanwhile, the classic p-type semiconductor P3HT is used for investigation as the host OSC, with its molecule structure shown in Figure 1b. Although TrTPFB and DMA-TPFB have similar molecular structures and identical anions, their doping mechanisms are

essentially different. As shown in Figure 1c, the doping mechanism of TrTPFB is based on electrophilic-attack reaction, with triphenylmethyl cations (Ph_3C^+) playing a major role[26]. Firstly, taking P3HT as an example, the stable intermediates are produced due to the electrophilic attack on P3HT by strong electrophiles Ph_3C^+. Subsequently, the stabilizing intermediate induces electron transfer from the neighboring neutral P3HT chain, generating neutral radical P3HT and radical cation P3HT (i.e., a polaron).

However, DMA-TPFB is supposed to operate following the protonation doping mechanism[22, 23] in which its cation protonates the P3HT chain by generating H^+, accompanied by the generation of intermediates. Similarly, the intermediate induces electron transfer from neighboring P3HT units, ultimately achieving p-doping, as shown in Figure 1d.

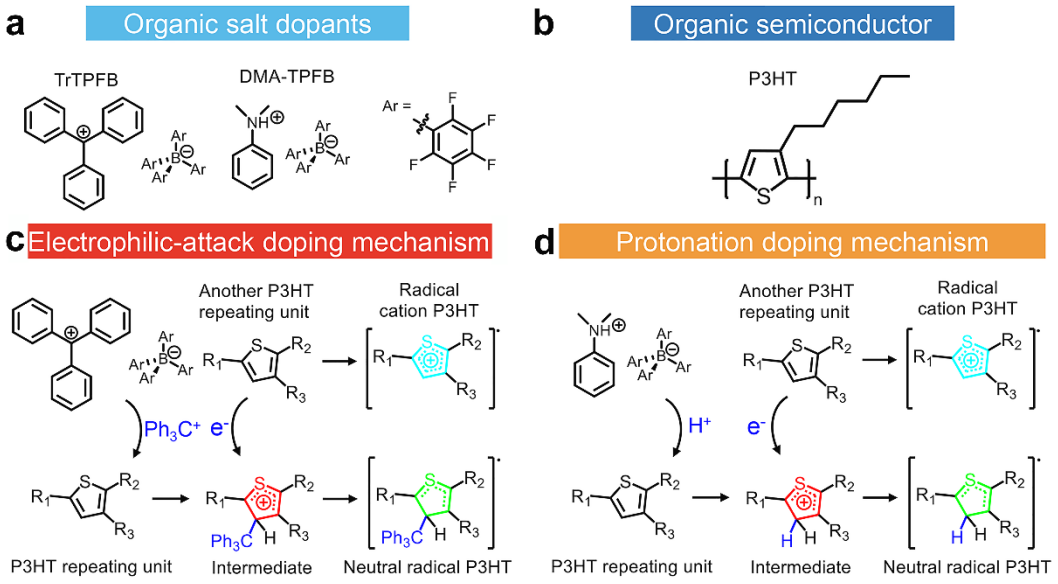

Figure 1. Dopant structures and doping mechanism. The molecular structure of (a) dopants (TrTPFB and DMA-TPFB) and (b) OSC P3HT. The doping mechanism for the two dopants: (c) electrophilic-attack doping mechanism for TrTPFB, and (d) protonation doping mechanism for DMA-TPFB.

To confirm the doping effect of TrTPFB and DMA-TPFB on P3HT, the electron spin resonance (ESR) spectroscopy is implemented on the doped films at room temperature, and the results are presented in Figure 2a. Both TrTPFB and DMA-TPFB

doped P3HT exhibit strong ESR signals compared to the pristine P3HT, indicating that both the two dopants can dope P3HT[46, 47].

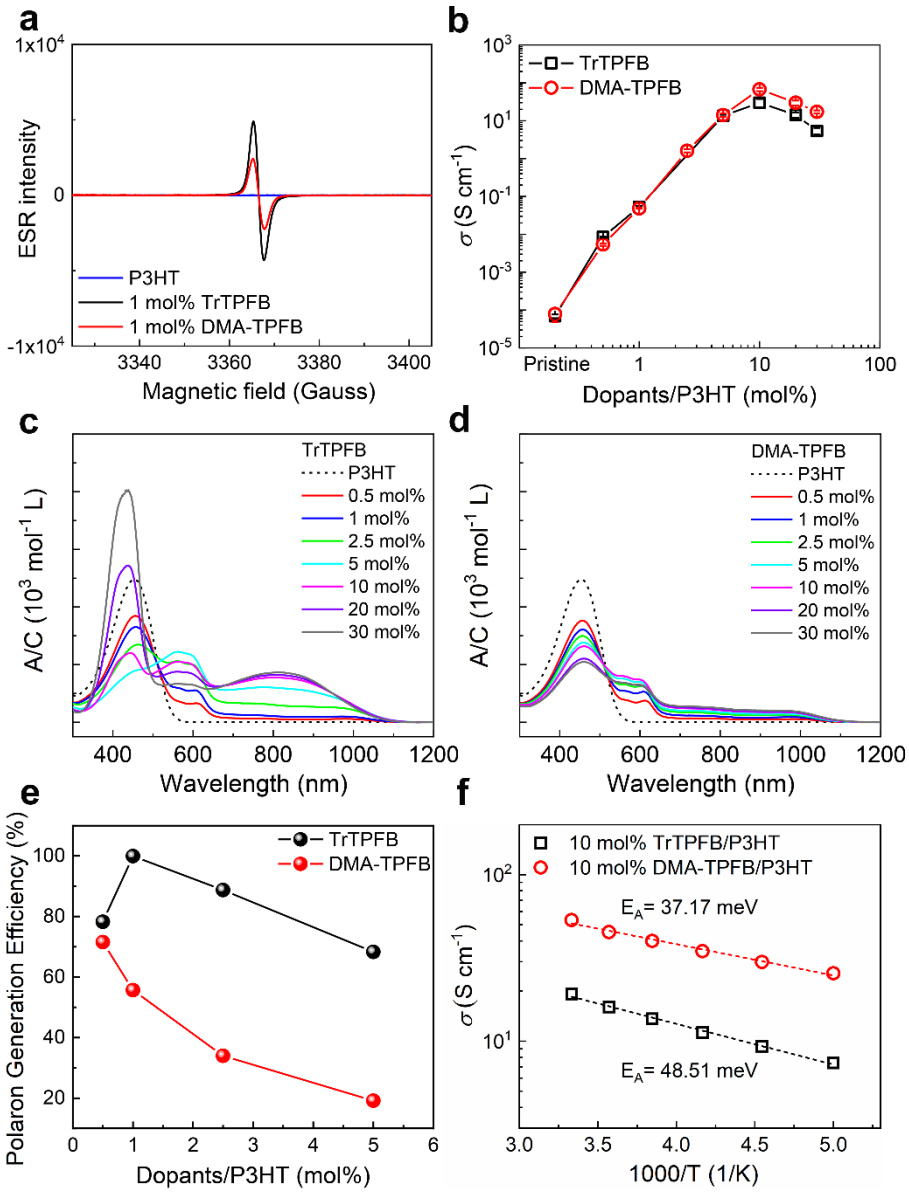

Figure 2. Characterization of doping effects of the two dopants. (a) The ESR spectra of P3HT films doped by TrTPFB and DMA-TPFB. (b) The electrical conductivity of P3HT films doped by TrTPFB and DMA-TPFB as a function of doping ratio. The UV-vis-NIR absorption spectra of doping P3HT solutions with increasing doping ratios: (c) TrTPFB and (d) DMA-TPFB (A/C indicates the ratio of absorption amplitude to P3HT concentration). (e) The polaron generation efficiency of TrTPFB and DMA-TPFB doped P3HT solutions at different doping ratios. (f) The activation energy extraction of 10 mol% TrTPFB and DMA-TPFB doped P3HT films based on temperature-dependent

electrical conductivity.

To further investigate the doping effect of the two dopants on P3HT, the electrical conductivity of the P3HT films with different doping ratios was measured. As shown in Figure 2b, the electrical conductivity of the pristine P3HT film is only 6.88×10^{-5} S cm^{-1}, while the electrical conductivity of the films increases rapidly with the introduction of the two dopants. The electrical conductivity of the two doped films reaches its maximum value at a doping ratio of 10 mol% (the molar ratio defines the molar proportion of dopant and polymer monomer), and then decreases as the doping ratio increases. For TrTPFB doped P3HT films, the maximum electrical conductivity increases by 6 orders of magnitude compared to the pristine P3HT, achieving 29.77 ± 7.73 S cm^{-1}, consistent with our previous results[26]. Remarkably, the maximum electrical conductivity of DMA-TPFB doped P3HT films reached 67.15± 6.93 S cm^{-1}, which is the record-high electrical conductivity for solution-doped P3HT (i.e., doping by mixing the solutions of semiconductor and dopant)[48-51].

2.2 Doping efficiency of TrTPFB and DMA-TPFB

To further understand the doping efficiency, quantitative UV-vis-NIR absorption spectroscopy measurements have been conducted on TrTPFB and DMA-TPFB doped P3HT solutions. As shown in Figure 2c, the pristine P3HT has only one intrinsic absorption peak located at around 454 nm. The intrinsic absorption peak of P3HT decreases gradually as the doping ratio of TrTPFB increases, while two broader absorption peaks appear in the range of about 500-1100 nm, attributed to the formation of polarons[52-54]. The intensity of these polaron absorption peaks increases rapidly with the increase of the doping ratio, and they almost remain unenhanced after the doping ratio reaches 10 mol%.

The UV-vis-NIR absorption spectra of the DMA-TPFB doped solutions exhibit a similar trend with the doping ratio to that of TrTPFB (see Figure 2d). However, the comparison reveals that the polaron absorption peaks of the TrTPFB doped samples are

significantly intense than those of DMA-TPFB, indicating that TrTPFB has a higher polaron generation efficiency. Additionally, we extracted the polaron absorption peak intensities by decomposing the spectra at different doping ratios, as exhibited in Figure S7. At a 5 mol% doping ratio, the intensity of the polaron absorption (at 776 nm or 1.60 eV) for TrTPFB is approximately twice that of DMA-TPFB, and at 10 mol% doping ratio, and the former is around three times higher than the latter. The polaron generation efficiency, quantitatively represented as the ratio between polaron concentration and dopant concentration, is further analyzed, with the results shown in Figure 2e (see Supporting Information for details). Notably, at equivalent doping ratios, the polaron generation efficiency of TrTPFB significantly surpasses that of DMA-TPFB.

A higher polaron generation efficiency indicates that a higher ratio of charge carrier pairs produced by doping. Charge carrier pairs form free carriers to increase electrical conductivity after separation[55, 56], and its separation ratio is expressed in terms of doping efficiency. For TrTPFB and DMA-TPFB, the production of charge carrier pairs is determined by their cations, and their separation depends mainly on their anions[26]. Since both dopants have the same anion, the higher polaron generation efficiency indicates higher doping efficiency. Therefore, it indicates that the doping efficiency of TrTPFB is much higher than that of DMA-TPFB in P3HT.

Interestingly, it is noted that the maximum electrical conductivity of the DMA-TPFB/P3HT film of 67.15 ± 6.93 S cm^{-1} is much higher than that of TrTPFB with 29.77 ± 7.73 S cm^{-1}. This raises the question of why DMA-TPFB achieves higher electrical conductivity than TrTPFB despite having a much lower doping efficiency. According to the equation $\sigma = ne\mu$, the electrical conductivity σ is jointly determined by the carrier concentration n and the carrier mobility μ. For doped OSCs, the carrier concentration depends on the doping efficiency dominantly. Despite DMA-TPFB having lower doping efficiency, i.e., lower carrier concentration, its doped OSC films obtain higher electrical conductivity, implying higher carrier mobility. Indeed, we implemented temperature-dependent electrical conductivity measurements on doped P3HT films. As

shown in Figure 2f, the electrical conductivity of the doped P3HT films increases with increasing temperature, which indicates the thermally activated transport behavior of the two doped P3HT films. The activation energies E_A of the two doped films were extracted according to the Arrhenius expression[57]. The E_A of TrTPFB and DMA-TPFB doped P3HT films (10 mol% doping ratio) were 37.17 meV and 48.51 meV, respectively. This difference suggests that charge transport in the former is less disrupted compared to the latter, indicating that the DMA-TPFB doped P3HT film exhibits higher mobility. Therefore, we assume that the electrical conductivity of doped films does not only depend on the doping efficiency of dopant; the effect of dopant on the microstructure of OSC film and, consequently, carrier mobility also plays a crucial role.

2.3 Effect of dopants on morphology/structure of P3HT films

To verify our assumption, we investigated the microstructural changes in the doped OSC films utilizing 2D GIWAXS. In Figure 3a, the GIWAXS pattern of the neat P3HT film indicates that the P3HT exhibits a predominantly edge-on orientation with some degree of orientation distribution. For the TrTPFB doped P3HT film, the GIWAXS pattern shows that the (100) peak is more distributed in the out-of-plane direction, indicating an increase in the edge-on oriented aggregates[58, 59], as shown in Figure 3b and 3d. Additionally, the (100) peak shifts to a lower value compared to that of the neat film, suggesting an increase in the real space lamellar packing distance (see Figure 3e). When examining the in-plane component, we observed the shifting of the (010) peak to a larger q value, indicating tighter π-π stacking in the TrTPFB doped film, as shown in Figures 3f and 3g. Furthermore, we noticed an increase in the full half maximum width (FWHM) of the (100) peak (see Figure 3e), indicating a decrease in the average P3HT crystalline grain size. Based on these results, we conclude that the TrTPFB dopants are mainly located between the alkyl chains of P3HT, increasing the lamellar spacing distance and inducing stronger π-π stacking, which is beneficial to

charge transport, [17] while reducing the average P3HT crystalline grain size.

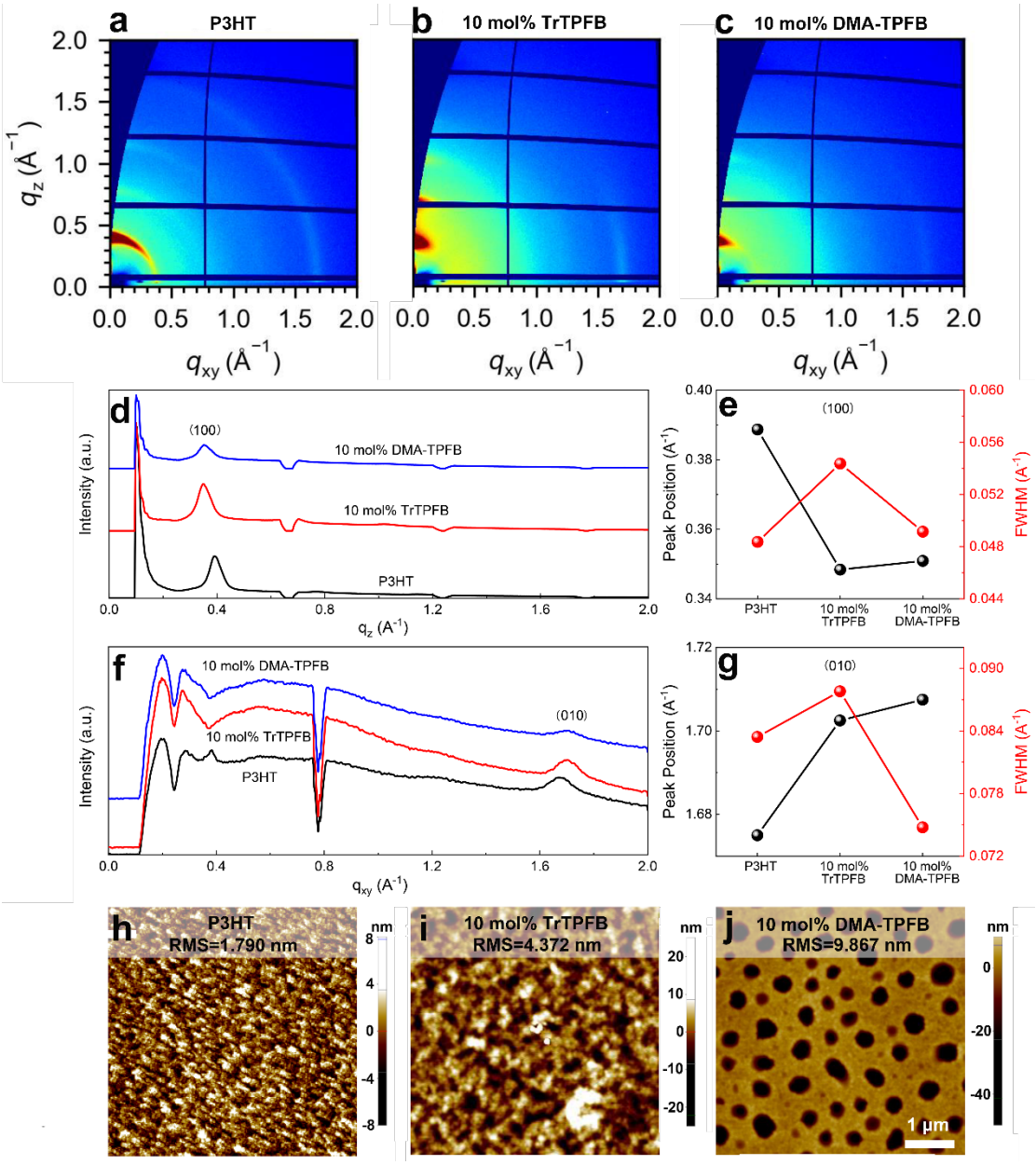

Figure 3. Characterize the microstructure and morphology of doped films. The 2D GIWAXS scattering images of (a) pristine P3HT, (b) 10 mol% TrTPFB, and (c) 10 mol% DMA-TPFB doped P3HT films. The linecuts of GIWAXS along the (d) q_z and (f) q_{xy} directions for 10 mol% TrTPFB and DMA-TPFB doped P3HT films. The variation of peak positions and FWHM of (e) (100) and (g) (010) peaks of TrTPFB and DMA-TPFB doped P3HT films. The AFM morphology of P3HT films: (h) pristine P3HT, (i) 10 mol% TrTPFB/P3HT, and (j) 10 mol% DMA-TPFB/P3HT.

For the DMA-TPFB doped P3HT film in Figure 3c, some similar features to the TrTPFB doped film were observed, such as an increase in lamellar spacing and closer π-π stacking (see Figure 3f and 3g). However, the FWHM of the (100) peak is smaller compared to that of TrTPFB doped P3HT (see Figure 3d and 3e), indicating a larger crystalline grain size or higher crystallinity. Thus, the DMA-TPFB doped film is supposed to have higher carrier mobility, supporting our above analysis.

Furthermore, we characterized the surface morphology of doped films by AFM. As shown in Figure 3h, the pristine P3HT film exhibits an irregular amorphous state with root mean square roughness (RMS) value of 1.790 nm. With the introduction of 10 mol% dopant TrTPFB, the P3HT film remains amorphous but its RMS value increases to 4.372 nm as shown in Figure 3i. However, upon the addition of 10 mol% DMA-TPFB dopant, the P3HT film demonstrates a uniform porous structure (see Figure 3j). The presence of porous structure leads to an increase in the RMS value of the film to 9.867 nm. The ordered porous structure is a feature showing the enhancement of crystallinity in DMA-TPFB doped P3HT compared to TrTPFB doped P3HT.

2.4 Investigations on doped PBBT-2T films

The results obtained from P3HT indicate that the dopant's influence on the microstructure of OSC films is crucial in determining the doping effect. Even though the dopant's efficiency is not high, it can still result in a strong doping effect (i.e., high electrical conductivity) by positively affecting the microstructure of OSC films. This is exactly the case with the DMA-TPFB dopant, as shown above. To explore the generalizability of this finding, we conducted comparable investigations with two dopants on another OSC, PBBT-2T (see molecular structure in Figure 4a).

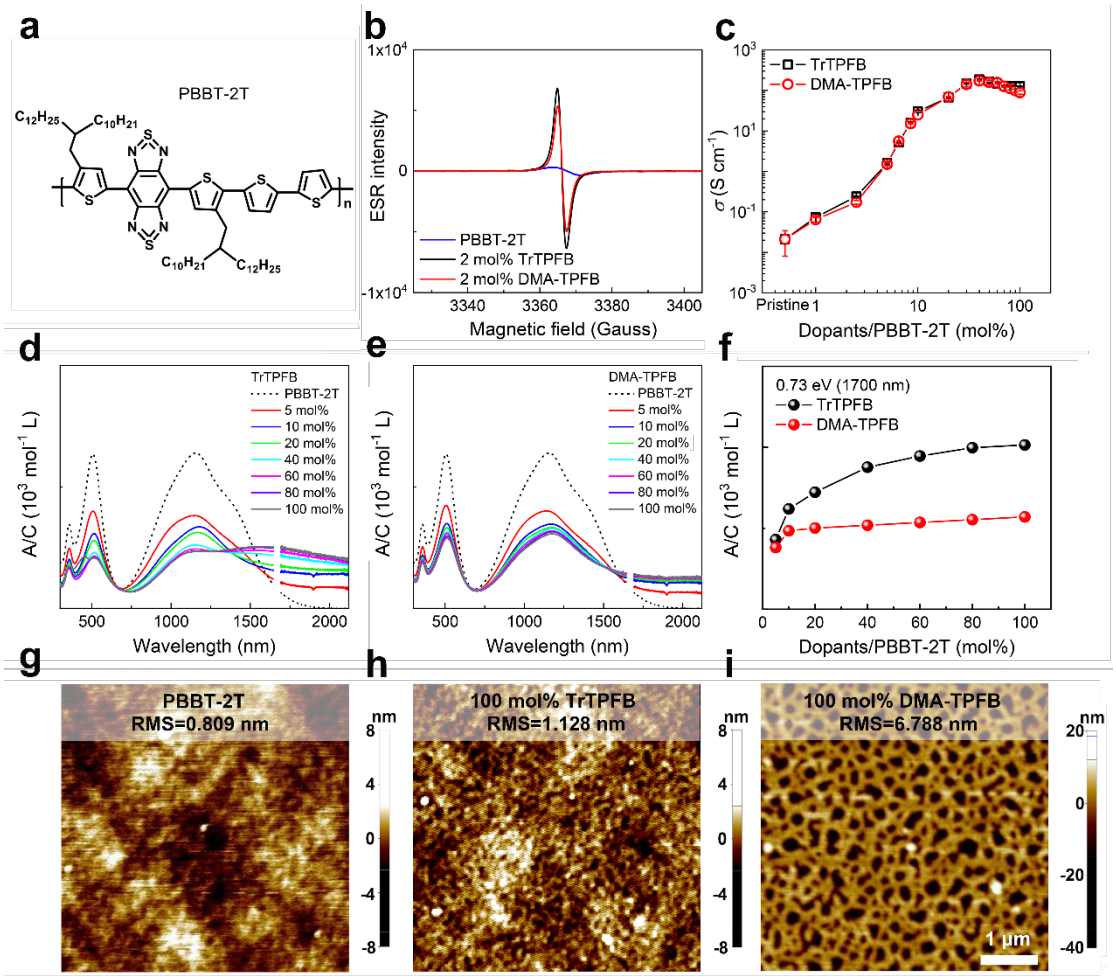

Figure 4. Characterization of doping effect and film morphology of doped PBBT-2T films. (a) The molecular structure of PBBT-2T. (b) The ESR spectra of PBBT-2T films doped by TrTPFB and DMA-TPFB. (c) The electrical conductivity of PBBT-2T films doped by TrTPFB and DMA-TPFB as a function of doping ratio. The UV-vis-NIR absorption spectra of doped PBBT-2T solutions with increasing doping ratios: (d) TrTPFB and (e) DMA-TPFB. (f) The polaron absorption peak intensities (the peak intensity was extracted from 1700 nm, i.e., 0.73 eV) of TrTPFB and DMA-TPFB doped PBBT-2T solutions at different doping ratios. The AFM morphology of PBBT-2T films: (g) pristine PBBT-2T, (h) 100 mol% TrTPFB/PBBT-2T, and (i) 100 mol% DMA-TPFB/PBBT-2T.

Figure 4b shows the ESR results of TrTPFB and DMA-TPFB doped PBBT-2T films, illustrating the doping effect of the two dopants on this semiconductor. Notably,

the pristine PBBT-2T film also exhibits a weak ESR signal, which may be due to the weak doping of PBBT-2T by oxygen despite the sealing treatment during the measurements[24]. As shown in Figure 4c, the electrical conductivity of PBBT-2T doped by TrTPFB increases with doping ratio up to 40 mol%, and thereafter slightly decreases. The maximum value of electrical conductivity is 186.7 ± 2.9 S cm^{-1} achieved at a doping ratio of 40 mol%. This represents an increase of about 4 orders of magnitude compared to the pristine PBBT-2T film with an electrical conductivity of about 0.02 ± 0.01 S cm^{-1}. The electrical conductivity of DMA-TPFB doped PBBT-2T films showed a similar trend to that of TrTPFB, with a maximum value of 172.8 ± 3.7 S cm^{-1} achieved at doping ratio of 40 mol%.

We then inspected the polaron generation efficiency of the two dopants in PBBT-2T. As shown in Figures 4d and 4e, the pristine PBBT-2T exhibits three primary intrinsic absorption peaks located at about 358 nm, 505 nm, and 1150 nm. In Figure 4d, the intrinsic absorption peak of PBBT-2T decreases with the increase of the doping ratio of TrTPFB, while a new absorption peak appears in the near-infrared region, attributed to the absorption peaks of the polarons produced by doping[60, 61]. The absorption peaks of the DMA-TPFB doped samples exhibit a similar trend to the TrTPFB doped samples, as shown in Figure 4e. However, the intensity of the polaron absorption (at 1700 nm or 0.73 eV) for TrTPFB is consistently higher than that of DMA-TPFB (see Figure 4f). These results are consistent with our observations in P3HT, and they again indicate that TrTPFB has a higher doping efficiency than DMA-TPFB.

Additionally, the morphology of the three PBBT-2T films was characterized by AFM. In Figure 4g, the pristine PBBT-2T film exhibits an amorphous state with a highly smooth surface of RMS = 0.829 nm. Despite the introduction of 100 mol% TrTPFB into the PBBT-2T film, the film maintains its amorphous state with a slight increase in RMS value to 1.128 nm, as shown in Figure 4h. Interestingly, the 100 mol% DMA-TPFB doped PBBT-2T film presents a porous structure with an increased RMS value of 6.788 nm (see Figure 4i). The appearance of porous structures and increased

RMS also supports the idea that DMA-TPFB doped film has higher crystallinity than the TrTPFB doped film, potentially leading to enhanced carrier mobility.

Overall, the results in doped PBBT-2T films again show that TrTPFB has a higher doping efficiency than DMA-TPFB, yet the latter has a more favorable effect on the microstructure of doped OSC films, leading to reduced structural disorder and more efficient charge transport.

2.5 Higher thermoelectric performance of doped OSCs enabled by DMA-TPFB compared to TrTPFB

One of the most important applications of dopants in OSCs is for thermoelectric devices. The power factor *PF* is a key metric in thermoelectric materials, quantifying their ability to convert a temperature gradient into electrical power. High *PF* is typically achieved through doping, which enhances electrical conductivity σ. However, increased σ often correlates with a higher carrier concentration, potentially diminishing the Seebeck coefficient *S*. The key to high thermoelectric performance is finding a balance between high σ and *S*. Ideally, doped OSC films should exhibit high mobility to boost σ without a corresponding significant decrease in the *S*. In OSCs, both *S* and σ are influenced by carrier mobility, which in turn is affected by the material's disorder. OSCs with greater mobility (or lower disorder) can experience a beneficial shift in the *S*-σ curve towards higher electrical conductivity values, leading to improved *PF* or enhanced thermoelectric performance[25, 62]. Thus, previous studies have focused on developing OSCs that can be doped to high levels and meanwhile retain high *S*. However, the influence of dopants on the disorder of the films and the consequent effect on thermoelectric performance have been rarely explored.

Our findings indicate that DMA-TPFB induces less disorder in OSCs than TrTPFB, suggesting potential superiority in thermoelectric performance when used as a dopant. To substantiate this hypothesis, we examined the *S* values of doped P3HT and PBBT-2T films with both dopants (further details in Supporting Information). Figures 5a and 5b show *S*, σ and *PF* as a function of doping ratio for TrTPFB and DMA-TPFB doped P3HT films, respectively. The σ of doped P3HT films first increases and then decreases with increasing doping ratio, while the *S* consistently declines for both dopants. A similar scenario is observed for TrTPFB and DMA-TPFB doped PBTT-2T

films, as shown in Figures 5c and 5d. Figure 5e presents the correlation between the *S* and σ in doped P3HT films. Notably, the *S* decreases with rising σ, a trend well-established in the literatures[63, 64]. Intriguingly, DMA-TPFB doped films exhibit a higher *S* than TrTPFB at identical σ levels. Similar results, *i.e.*, the higher *S* of DMA-TPFB doped films than that of the TrTPFB doped ones at the same σ, are also observed in PBBT-2T films. These results directly demonstrate the shift of the *S*-σ curve towards higher σ in DMA-TFPB doped films due to the lower disorder in them.

The peak *PF* values of the doped P3HT and PBBT-2T films are depicted in Figure 5f. DMA-TPFB doping achieves higher *PF* values than TrTPFB within the same OSC films, an expected outcome of the altered *S*-σ curve, or more fundamentally, the diminished disorder in DMA-TPFB doped films. These findings are pivotal for the development of high-performance dopants in OTEs, underscoring the importance of not just dopant efficiency but also the minimization of induced disorder in the doped films.

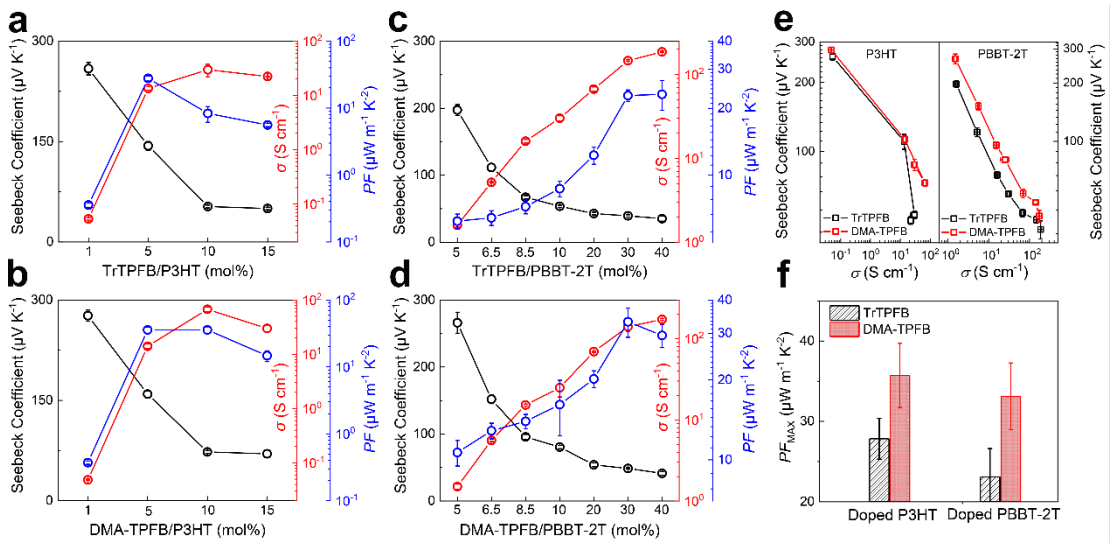

Figure 5. Characterization of thermoelectric performance of doped OSC devices. The electrical conductivity, Seebeck coefficient, and power factor of OSC films doped with two dopants as a function of doping ratio: (a) TrTPFB/P3HT, (b) DMA-TPFB/P3HT, (c) TrTPFB/PBBT-2T, (d) DMA-TPFB/PBBT-2T. (e) The *S*-σ relationship for TrTPFB and DMA-TPFB doped films. (f) The maximum *PF* of thermoelectric devices composed of TrTPFB and DMA-TPFB doped OSCs.

CONCLUSION

To summarize, this work investigated the impact of two organic dopants, TrTPFB and DMA-TPFB, on the doping properties and microstructure of P3HT and PBBT-2T films. The study revealed that while TrTPFB has a higher doping efficiency, films doped with DMA-TPFB displayed superior electrical conductivity. This counterintuitive result was attributed to DMA-TPFB's ability to induce greater crystallinity and lower structural disorder in the films, thereby facilitating better charge transport. More interestingly, DMA-TPFB was found to result in higher thermoelectric performance than TrTPFB in the same host semiconductor because DMA-TPFB improves film structures. These findings underscore the significance of a dopant's impact on film microstructure in determining the electrical and thermoelectric properties of doped OSC films. The study points out strategies for improving dopant performance by tailoring their effects on film microstructure.

Methods

Preparation of doped solutions and OSC films:

The dopants TrTPFB (from Strem Chemicals, Inc.), DMA-TPFB (from TCI (Shanghai) Development Co, Ltd.) and the organic semiconductors P3HT (from Aladdin Reagent Co., Ltd.) and PBBT-2T were dissolved in chlorobenzene (CB, from Sigma Aldrich, Inc.) to form solutions with concentrations of 10 g L^{-1}, 5 g L^{-1}, 10 g L^{-1}, and 5 g L^{-1}, respectively. All solutions were filtered through a 0.45 μm syringe filter to remove impurities or aggregates prior to usage. The PBBT-2T solution needs to be preheated at 60 °C for two hours before usage. The doping solutions were prepared by blending the dopant and the OSC solutions in a predetermined ratio. The doped films were prepared by spin-coating the doping solutions at 1500 rpm s^{-1} for 30 s, and then the films were annealed at 130 ℃ for 5 min for P3HT and at 100 ℃ for 10 min for PBBT-2T.

UV-vis-NIR, ESR, and AFM measurements:

The ultraviolet-visible-near-infrared (UV-vis-NIR) absorption spectra of PBBT-2T doped solutions with varied doping ratio were determined by UV-3600PLUS

(SHIMADZU). The ESR measurements of doped films were carried out at room temperature on a JEOL JES-FA200 ESR spectrometer. Prior to the ESR measurements, the doped films were prepared on glass substrates by the spin-coating method and then sealed in paramagnetic tubes after annealing treatment. The morphology of the doped films was investigated by AFM in non-contact mode on a Park XE-7 System.

Measurement of electrical conductivity:

To measure the electrical conductivity of doped films, the doping solutions were spin-coated at 1500 rpm s^{-1} for 30 s on silicon wafers with 300 nm SiO_2, on which patterned electrodes (Cr/Au: 2 nm/30 nm) were prepared by photolithography. The electrical conductivity of the doped films was then measured in the air using a Keithley 4200 semiconductor analyzer by the four-probe method, and the device structure and specific measurements were shown in Supporting Information Figure S2.

Characterization of thermoelectric performance*:*

The Seebeck coefficients of the doped films were obtained by a homemade thermoelectric measuring device containing a heater and two thermometers, which also acted as electrical contacts, made by photolithographically patterning a metallic bilayer of chromium (10 nm) and gold (15 nm) on a glass substrate. The Seebeck coefficient measurements were performed according to the equation $S = \frac{\Delta V}{\Delta T}$. The temperature gradient was estimated between the two electrodes by converting the electrode resistance to temperature via the temperature coefficient of resistance (TCR)[7] (see Supporting Information Figure S12 and S13), and the thermopotential difference was measured using a Keithley 2182A. The Seebeck coefficient was measured using a Janis ST-100 at 300 K in a high vacuum ($<10^{-5}$ mbar).

ACKNOWLEDGMENT

We thank the Center for Analysis and Testing of Hunan University for providing the AFM. Y. Hu thanks the National Key Research and Development Program (2022YFB3603802), the National Natural Science Foundation of China (62222403; 62074054; U21A20497), Natural Science Foundation of Hunan Province (2022JJ10019), and Shenzhen Science and Technology Innovation Commission (RCYX20200714114537036) for financial support. S.W. acknowledges funding support from Agence Nationale de la Recherche (ANR-23-CPJ1-0047-01). J. Guo acknowledges the support from Fundamental Research Program in Shanxi Province (No. 202303021212159).

REFERENCES

[1] Y. Kim, S. Chung, K. Cho, D. Harkin, W. T. Hwang, D. Yoo, J. K. Kim, W. Lee, Y. Song, H. Ahn, *Adv. Mater.* **2019**, *31*, 1806697.

[2] S. E. Yoon, J. Park, J. E. Kwon, S. Y. Lee, J. M. Han, C. Y. Go, S. Choi, K. C. Kim, H. Seo, J. H. Kim, B. G. Kim, *Adv. Mater.* **2020**, *32*, 2005129.

[3] D. Lu, F. Huang, C. Gao, J. Yang, J. Guo, Y. Hu, Q. Bao, Y. Y. Noh, J. Chu, W. Li, *Adv. Funct. Mater.* **2022**, *32*, 2111285.

[4] H. Guo, C. Y. Yang, X. Zhang, A. Motta, K. Feng, Y. Xia, Y. Shi, Z. Wu, K. Yang, J. Chen, Q. Liao, Y. Tang, H. Sun, H. Y. Woo, S. Fabiano, A. Facchetti, X. Guo, *Nature* **2021**, *599*, 67-73.

[5] T. He, M. Stolte, Y. Wang, R. Renner, P. P. Ruden, F. Würthner, C. D. Frisbie, *Nat. Mater.* **2021**, *20*, 1532-1538.

[6] H. Wei, Z. Cheng, T. Wu, Y. Liu, J. Guo, P. A. Chen, J. Xia, H. Xie, X. Qiu, T. Liu, B. Zhang, J. Hui, Z. Zeng, Y. Bai, Y. Hu, *Adv. Mater.* **2023**, *35*, 2300084.

[7] H. Wei, P. A. Chen, J. Guo, Y. Liu, X. Qiu, H. Chen, Z. Zeng, T. Q. Nguyen, Y. Hu, *Adv. Funct. Mater.* **2021**, *31*, 2102768.

[8] J. Liu, B. van der Zee, R. Alessandri, S. Sami, J. Dong, M. I. Nugraha, A. J. Barker, S. Rousseva, L. Qiu, X. Qiu, N. Klasen, R. C. Chiechi, D. Baran, M. Caironi, T. D. Anthopoulos, G. Portale, R. W. A. Havenith, S. J. Marrink, J. C. Hummelen, L. J. A. Koster, *Nat. Commun.* **2020**, *11*, 5694.

[9] K. Feng, W. Yang, S. Y. Jeong, S. Ma, Y. Li, J. Wang, Y. Wang, H. Y. Woo, P. K. L. Chan, G. Wang, X. Guo, M. Zhu, *Adv. Mater.* **2023**, *35*, 2210847.

[10] C. Y. Yang, Y. F. Ding, D. Huang, J. Wang, Z. F. Yao, C. X. Huang, Y. Lu, H. I. Un, F. D. Zhuang, J. H. Dou, C. A. Di, D. Zhu, J. Y. Wang, T. Lei, J. Pei, *Nat.*

Commun. **2020**, *11*, 3292.
[11] B. Russ, A. Glaudell, J. J. Urban, M. L. Chabinyc, R. A. Segalman, *Nat. Rev. Mater.* **2016**, *1*, 1-14.
[12] L. Deng, Y. Liu, Y. Zhang, S. Wang, P. Gao, *Adv. Funct. Mater.* **2023**, *33*, 2210770.
[13] H. Méndez, G. Heimel, S. Winkler, J. Frisch, A. Opitz, K. Sauer, B. Wegner, M. Oehzelt, C. Röthel, S. Duhm, D. Többens, N. Koch, I. Salzmann, *Nat. Commun.* **2015**, *6*, 8560.
[14] Y. Karpov, T. Erdmann, M. Stamm, U. Lappan, O. Guskova, M. Malanin, I. Raguzin, T. Beryozkina, V. Bakulev, F. Günther, S. Gemming, G. Seifert, M. Hambsch, S. Mannsfeld, B. Voit, A. Kiriy, *Macromolecules* **2017**, *50*, 914-926.
[15] Y. Karpov, T. Erdmann, I. Raguzin, M. Al-Hussein, M. Binner, U. Lappan, M. Stamm, K. L. Gerasimov, T. Beryozkina, V. Bakulev, D. V. Anokhin, D. A. Ivanov, F. Günther, S. Gemming, G. Seifert, B. Voit, R. Di Pietro, A. Kiriy, *Adv. Mater.* **2016**, *28*, 6003-6010.
[16] D. Kiefer, R. Kroon, A. I. Hofmann, H. Sun, X. Liu, A. Giovannitti, D. Stegerer, A. Cano, J. Hynynen, L. Yu, Y. Zhang, D. Nai, T. F. Harrelson, M. Sommer, A. J. Moule, M. Kemerink, S. R. Marder, I. McCulloch, M. Fahlman, S. Fabiano, C. Muller, *Nat. Mater.* **2019**, *18*, 149-155.
[17] Y. Liu, B. Nell, K. Ortstein, Z. Wu, Y. Karpov, T. Beryozkina, S. Lenk, A. Kiriy, K. Leo, S. Reineke, *ACS Appl. Mater. Interfaces* **2019**, *11*, 11660-11666.
[18] E. H. Suh, J. G. Oh, J. Jung, S. H. Noh, T. S. Lee, J. Jang, *Adv. Energy Mater.* **2020**, *10*, 2002521.
[19] J. Panidi, A. F. Paterson, D. Khim, Z. Fei, Y. Han, L. Tsetseris, G. Vourlias, P. A. Patsalas, M. Heeney, T. D. Anthopoulos, *Adv. Sci.* **2018**, *5*, 1700290.
[20] A. F. Paterson, L. Tsetseris, R. Li, A. Basu, H. Faber, A. H. Emwas, J. Panidi, Z. Fei, M. R. Niazi, D. H. Anjum, M. Heeney, T. D. Anthopoulos, *Adv. Mater.* **2019**, *31*, 1900871.
[21] Q. Hu, E. Rezaee, M. Li, Q. Chen, C. Li, S. Cai, H. Shan, Z. X. Xu, *Sol. RRL* **2020**, *4*, 1900340.
[22] B. Wegner, D. Lungwitz, A. E. Mansour, C. E. Tait, N. Tanaka, T. Zhai, S. Duhm, M. Forster, J. Behrends, Y. Shoji, A. Opitz, U. Scherf, E. J. W. List-Kratochvil, T. Fukushima, N. Koch, *Adv. Sci.* **2020**, *7*, 2001322.
[23] P. S. Marqués, G. Londi, B. Yurash, T. Q. Nguyen, S. Barlow, S. R. Marder, D. Beljonne, *Chem. Sci.* **2021**, *12*, 7012-7022.
[24] Y. Hu, Z. D. Rengert, C. McDowell, M. J. Ford, M. Wang, A. Karki, A. T. Lill, G. C. Bazan, T. Q. Nguyen, *ACS Nano* **2018**, *12*, 3938-3946.
[25] J. Guo, G. Li, H. Reith, L. Jiang, M. Wang, Y. Li, X. Wang, Z. Zeng, H. Zhao, X. Lu, G. Schierning, K. Nielsch, L. Liao, Y. Hu, *Adv. Electron. Mater.* **2020**, *6*, 1900945.
[26] J. Guo, Y. Liu, P. A. Chen, X. Wang, Y. Wang, J. Guo, X. Qiu, Z. Zeng, L. Jiang, Y. Yi, S. Watanabe, L. Liao, Y. Bai, T. Q. Nguyen, Y. Hu, *Adv. Sci.* **2022**, *9*,

2203111.
[27] Z. Ke, M. H. Ahmed, A. Abtahi, S. H. Hsu, W. Wu, M. F. Espenship, K. N. Baustert, K. R. Graham, J. Laskin, L. Pan, J. Mei, *Adv. Funct. Mater.* **2023**, *33*, 2211522.
[28] D. Neusser, C. Malacrida, M. Kern, Y. M. Gross, J. van Slageren, S. Ludwigs, *Chem. Mater.* **2020**, *32*, 6003-6013.
[29] Y. Yamashita, J. Tsurumi, M. Ohno, R. Fujimoto, S. Kumagai, T. Kurosawa, T. Okamoto, J. Takeya, S. Watanabe, *Nature* **2019**, *572*, 634-638.
[30] H. I. Un, S. A. Gregory, S. K. Mohapatra, M. Xiong, E. Longhi, Y. Lu, S. Rigin, S. Jhulki, C. Y. Yang, T. V. Timofeeva, J. Y. Wang, S. K. Yee, S. Barlow, S. R. Marder, J. Pei, *Adv. Energy Mater.* **2019**, *9*, 1900817.
[31] I. E. Jacobs, Y. Lin, Y. Huang, X. Ren, D. Simatos, C. Chen, D. Tjhe, M. Statz, L. Lai, P. A. Finn, W. G. Neal, G. D'Avino, V. Lemaur, S. Fratini, D. Beljonne, J. Strzalka, C. B. Nielsen, S. Barlow, S. R. Marder, I. McCulloch, H. Sirringhaus, *Adv. Mater.* **2021**, *34*, 2102988.
[32] D. Scheunemann, E. Järsvall, J. Liu, D. Beretta, S. Fabiano, M. Caironi, M. Kemerink, C. Müller, *Chem. Phys. Rev.* **2022**, *3*, 021309.
[33] J. E. Cochran, M. J. N. Junk, A. M. Glaudell, P. L. Miller, J. S. Cowart, M. F. Toney, C. J. Hawker, B. F. Chmelka, M. L. Chabinyc, *Macromolecules* **2014**, *47*, 6836-6846.
[34] P. Y. Yee, D. T. Scholes, B. J. Schwartz, S. H. Tolbert, *J. Phys. Chem. Lett.* **2019**, *10*, 4929-4934.
[35] B. Neelamraju, K. E. Watts, J. E. Pemberton, E. L. Ratcliff, *J. Phys. Chem. Lett.* **2018**, *9*, 6871-6877.
[36] E. M. Thomas, E. C. Davidson, R. Katsumata, R. A. Segalman, M. L. Chabinyc, *ACS Macro Lett.* **2018**, *7*, 1492-1497.
[37] Y. Zhong, V. Untilova, D. Muller, S. Guchait, C. Kiefer, L. Herrmann, N. Zimmermann, M. Brosset, T. Heiser, M. Brinkmann, *Adv. Funct. Mater.* **2022**, *32*, 2202075.
[38] O. Zapata-Arteaga, A. Perevedentsev, S. Marina, J. Martin, J. S. Reparaz, M. Campoy-Quiles, *ACS Energy Lett.* **2020**, *5*, 2972-2978.
[39] R. Hanus, S. A. Gregory, M. J. Adams, S. Graham, S. K. Yee, *Adv. Electron. Mater.* **2022**, *8*, 2200846.
[40] E. M. Thomas, K. A. Peterson, A. H. Balzer, D. Rawlings, N. Stingelin, R. A. Segalman, M. L. Chabinyc, *Adv. Electron. Mater.* **2020**, *6*, 2000595.
[41] S. N. Patel, A. M. Glaudell, D. Kiefer, M. L. Chabinyc, *ACS Macro Lett.* **2016**, *5*, 268-272.
[42] O. Zapata-Arteaga, B. Dörling, A. Perevedentsev, J. Martín, J. S. Reparaz, M. Campoy-Quiles, *Macromolecules* **2020**, *53*, 609-620.
[43] S. N. Patel, A. M. Glaudell, K. A. Peterson, E. M. Thomas, K. A. O'Hara, E. Lim, M. L. Chabinyc, *Sci. Adv.* **2017**, *3*, e1700434.
[44] I. E. Jacobs, E. W. Aasen, J. L. Oliveira, T. N. Fonseca, J. D. Roehling, J. Li, G.

Zhang, M. P. Augustine, M. Mascal, A. J. Moulé, *J. Mater. Chem. C* **2016**, *4*, 3454-3466.
[45] I. E. Jacobs, C. Cendra, T. F. Harrelson, Z. I. Bedolla Valdez, R. Faller, A. Salleo, A. J. Moulé, *Mater. Horiz.* **2018**, *5*, 655-660.
[46] Y. Chen, L. Zhao, P. A. Chen, Y. Li, J. Guo, Y. Liu, X. Qiu, J. Xia, K. Chen, H. Chen, X. Lu, L. Jiang, L. Liao, T. Q. Nguyen, Y. Hu, *Matter* **2022**, *5*, 2882-2897.
[47] X. Qiu, J. Guo, P. A. Chen, K. Chen, Y. Liu, C. Ma, H. Chen, Y. Hu, *Small* **2021**, *17*, 2101325.
[48] D. T. Duong, C. Wang, E. Antono, M. F. Toney, A. Salleo, *Org. Electron.* **2013**, *14*, 1330-1336.
[49] J. Hynynen, D. Kiefer, L. Yu, R. Kroon, R. Munir, A. Amassian, M. Kemerink, C. Muller, *Macromolecules* **2017**, *50*, 8140-8148.
[50] E. Lim, K. A. Peterson, G. M. Su, M. L. Chabinyc, *Chem. Mater.* **2018**, *30*, 998-1010.
[51] J. Kim, J. Guo, G. Sini, M. K. Sørensen, J. W. Andreasen, K. L. Woon, V. Coropceanu, S. H. K. Paleti, H. Wei, S. Peralta, M. Mallouki, C. Müller, Y. Hu, T.-T. Bui, S. Wang, *Mater. Today Adv.* **2023**, *18*, 100360.
[52] M. Arvind, C. E. Tait, M. Guerrini, J. Krumland, A. M. Valencia, C. Cocchi, A. E. Mansour, N. Koch, S. Barlow, S. R. Marder, J. Behrends, D. Neher, *J. Phys. Chem. B* **2020**, *124*, 7694-7708.
[53] C. Wang, D. T. Duong, K. Vandewal, J. Rivnay, A. Salleo, *Phys. Rev. B* **2015**, *92*, 119901.
[54] L. Müller, D. Nanova, T. Glaser, S. Beck, A. Pucci, A. K. Kast, R. R. Schröder, E. Mankel, P. Pingel, D. Neher, W. Kowalsky, R. Lovrincic, *Chem. Mater.* **2016**, *28*, 4432-4439.
[55] M. L. Tietze, J. Benduhn, P. Pahner, B. Nell, M. Schwarze, H. Kleemann, M. Krammer, K. Zojer, K. Vandewal, K. Leo, *Nat. Commun.* **2018**, *9*, 1182.
[56] A. Privitera, R. Warren, G. Londi, P. Kaienburg, J. Liu, A. Sperlich, A. E. Lauritzen, O. Thimm, A. Ardavan, D. Beljonne, M. Riede, *J. Mater. Chem. C* **2021**, *9*, 2944-2954.
[57] A. M. Glaudell, J. E. Cochran, S. N. Patel, M. L. Chabinyc, *Adv. Energy Mater.* **2015**, *5*, 1401072.
[58] Y. Xiao, X. Lu, *Mater. Today Nano* **2019**, *5*, 100030.
[59] K. Kang, S. Watanabe, K. Broch, A. Sepe, A. Brown, I. Nasrallah, M. Nikolka, Z. Fei, M. Heeney, D. Matsumoto, K. Marumoto, H. Tanaka, S. I. Kuroda, H. Sirringhaus, *Nat. Mater.* **2016**, *15*, 896-902.
[60] T. L. D. Tam, G. Wu, S. W. Chien, S. F. V. Lim, S. W. Yang, J. Xu, *ACS Mater. Lett.* **2020**, *2*, 147-152.
[61] P.-A. Chen, J. Guo, X. Yan, Y. Liu, H. Wei, X. Qiu, J. Xia, J. Guo, J. Ding, Z. Gong, C. Chen, T. Lei, H. Chen, Z. Zeng, Y. Hu, *Small* **2023**, *19*, 2207858.
[62] S. D. Kang, G. J. Snyder, *Nat. Mater.* **2017**, *16*, 252-257.
[63] C. Chen, I. E. Jacobs, K. Kang, Y. Lin, C. Jellett, B. Kang, S. B. Lee, Y. Huang,

M. BaloochQarai, R. Ghosh, M. Statz, W. Wood, X. Ren, D. Tjhe, Y. Sun, X. She, Y. Hu, L. Jiang, F. C. Spano, I. McCulloch, H. Sirringhaus, *Adv. Energy Mater.* **2023**, *13*, 2202797.

[64] J. Tang, J. Ji, R. Chen, Y. Yan, Y. Zhao, Z. Liang, *Adv. Sci.* **2022**, *9*, 2103646.